ADVANCED MATERIALS INTERFACES
www.advmatinterfaces.de

Impact of Different Intermediate Layers on the Morphology and Crystallinity of TiO_2 Grown on Carbon Nanotubes by Atomic Layer Deposition

Jiao Wang, Zhigang Yin, Felix Hermerschmidt, Emil J. W. List-Kratochvil, and Nicola Pinna**

Nanocomposites of TiO_2 and carbon nanotubes (CNTs) have been extensively studied in photocatalysis, sensing, and energy conversion and storage over the last decade. The unique properties of these nanocomposites are greatly dependent on the morphology, crystallinity, and homogeneity of the TiO_2 coating. However, a fine control of the film microstructure is still challenging due to limited understanding of early stages of the TiO_2 growth. The presence of an intermediate buffer layer can induce remarkable changes in the morphological and structural characteristics of the coatings. Here, TiO_2 films deposited by atomic layer deposition (ALD) on CNTs without and with different intermediate layers (Al_2O_3 and ZnO) have been systematically investigated. Compared to bare CNTs, it is suggested that these two intermediate layers with higher surface energy can lead to a delay of the TiO_2 crystallization, ultimately resulting in the growth of conformal and crystalline TiO_2 films. This study demonstrates a strategy to tailor the microstructure and the properties of thin films via ALD by applying intermediate layers and provides information about the role of surface energy of the substrate in crystallization and growth behavior of ALD thin films.

1. Introduction

Nanocomposites of TiO_2 and carbon nanotubes (CNTs), such as TiO_2/CNTs heterostructures, have attracted great interest owing to their unique structures and outstanding properties.[1] As a wide bandgap semiconductor (3.2 eV for anatase), TiO_2 has been widely studied in solar cells, gas sensors, and energy storage and conversion due to its good chemical stability, excellent optoelectronic properties, low cost, and environmental friendliness.[2] Meanwhile, CNTs are 1D nanostructures with interesting features such as large surface area and high electrical and thermal conductivities.[3] CNTs are ideal supports for various metal oxide coatings to synthesize advanced composite nanostructures and promote their photocatalytic, electrical, electrochemical, and sensing properties. For example, CNTs can enhance the separation and transfer of photogenerated carriers and improve the photocatalytic efficiency of TiO_2.[1b] Therefore, many efforts have been made on the synthesis of TiO_2 and CNTs nanocomposites to improve the performance and to understand the underlying mechanisms.[4]

The unique properties of TiO_2/CNTs nanocomposites are largely dependent on the morphology and crystallinity of the TiO_2 films.[5] So far, there have been a variety of techniques used to deposit TiO_2 onto CNTs, including molecular beam epitaxy (MBE), atomic layer deposition (ALD), metal organic chemical vapor deposition (MOCVD), inkjet printing and sol–gel techniques.[6] ALD is a thin film deposition technique based on self-limiting surface reactions, allowing to coat high aspect ratio substrates with a fine control of the thickness and morphology of the deposited films.[7] Therefore, ALD has been widely used to grow various metal/metal oxides thin films with controllable thicknesses and compositions.[8] The properties of core–shell TiO_2/CNTs nanostructures synthesized by ALD have been reported by mainly focusing on the effects of process parameters such as precursors pulse time, temperature of the reaction chamber and number of ALD cycles.[2a,4a,5,9] However, there are very limited studies that explore the nucleation behavior and growth mechanisms of ALD-grown TiO_2 films.[10] It has been demonstrated that the nucleation of TiO_2 film is affected by the deposition conditions such as nature of the

J. Wang, Prof. Z. Yin, Prof. N. Pinna
Institut für Chemie and IRIS Adlershof
Humboldt-Universität zu Berlin
Brook-Taylor-Str. 2, 12489 Berlin, Germany
E-mail: yinzhg@fjirsm.ac.cn; nicola.pinna@hu-berlin.de
Prof. Z. Yin
State Key Laboratory of Structural Chemistry
Fujian Institute of Research on the Structure of Matter
Chinese Academy of Sciences
155 Yangqiao West Road, Fuzhou, Fujian 350002, China
Dr. F. Hermerschmidt, Prof. E. J. W. List-Kratochvil
Institut für Physik
Institut für Chemie and IRIS Adlershof
Humboldt-Universität zu Berlin
Zum Großen Windkanal 2, 12489 Berlin, Germany
Prof. E. J. W. List-Kratochvil
Helmholtz-Zentrum Berlin für Materialien und Energie GmbH
Hahn-Meitner-Platz 1, 14109 Berlin, Germany
The ORCID identification number(s) for the author(s) of this article can be found under https://doi.org/10.1002/admi.202100759.

DOI: 10.1002/admi.202100759

precursors, temperature, number of ALD cycles, as well as the nature and density of surfaces species of the substrate.[3,11] For example, our group has already studied the role of functional surface groups and defect sites on functionalized CNTs, which act as anchoring and nucleation sites for the initiation of film growth by ALD.[4a] As a matter of fact, the nucleation behavior of ALD-grown films was demonstrated to strongly correlate to the chemical and structural properties of the substrate.[11e,12] As a result, different substrates can alter the film properties and provide a simple strategy to tune its morphology and microstructure. There are principally two approaches to modify the surface of the substrate: one is the application of a chemical or physical treatment to the surface and the other is the deposition of a buffer layer.[10,13] The existence of one or more intermediate layers plays an important role in the morphological and structural characteristics of the coating, ultimately affecting the chemical and physical properties of the nanostructure. For example, Amar et al. reported that the surface atom diffusion constant regulates the coverage of a submonolayer film.[14] According to the adatom diffusion equation $D = D_0 \exp(-E_a/kT)$, the diffusion constant (D) is related to the activation energy E_a for surface diffusion. Therefore, different buffer layers can lead to different substrate coverage. Piltaver et al. showed that the grain size of polycrystalline TiO_2 can be controlled by introducing a thin Al_2O_3 buffer layer.[15] Furthermore, Puurunen et al. studied the growth and crystallite sizes of an ALD TiO_2 films on planar Si wafers with different interlayers (SiO_2 and Al_2O_3).[16] Sun et al. deposited conformal TiO_2 films on CNTs by employing an ultrathin Al_2O_3 adhesion layer for applications in energy storage devices.[17] However, the mechanism and effect of intermediate layers on the crystallization and growth behavior of ALD-grown TiO_2 films are still not clearly understood.

ALD-grown films are normally thin (≪100 nm), and therefore the surface energy plays a key role in the total energy of the system.[11a] It can be anticipated that the surface energy of the intermediate layers is one of the most important factors that influences the nucleation process of TiO_2 thin films. The nucleation and the initial deposition steps can further control the characteristics of subsequent grown films, including their morphology and crystallinity. To the best of our knowledge, there is no study discussing the effect of different intermediate layers on the morphology, crystallinity and homogeneity of TiO_2 films onto CNTs. In particular, although a large amount of work has been focused on depositing uniform metal oxide coatings on CNTs by ALD, it is still difficult to obtain conformal and crystalline TiO_2 films.

Herein, TiO_2 films with various thicknesses are deposited by ALD directly onto bare CNTs and onto CNTs modified with Al_2O_3 or ZnO intermediate layers. The effects of these intermediate layers on the crystallization and growth behavior of TiO_2 films are systematically studied. The morphology and crystallinity of the resulting films are characterized, while the surface energies of the substrates were studied by contact angle measurements. This work not only provides insights into the role of intermediate layers on the morphology and crystallinity of metal-oxide ALD films, but also introduces a promising strategy to understand fundamental aspects as well as to develop well-tailored nanocomposites for a variety of applications.

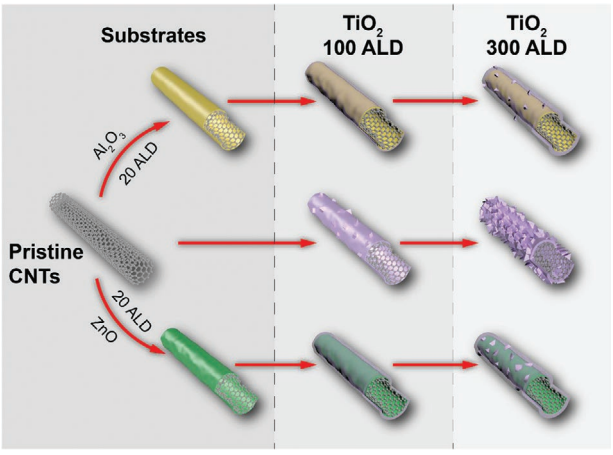

Figure 1. Schematic view of the synthesis processes for 100 and 300 ALD cycles of TiO_2 deposited on pristine CNTs, Al_2O_3/CNTs, and ZnO/CNTs substrates at 240 °C, respectively.

2. Results and Discussion

2.1. Nucleation Process

Figure 1 illustrates a schematic view of the synthesis processes for three types of TiO_2/CNT-based nanocomposites, namely, TiO_2/CNTs, TiO_2/Al_2O_3/CNTs, and TiO_2/ZnO/CNTs. 100 and 300 ALD cycles were used to clearly show the effects of the intermediate layers on the crystallinity and growth behavior of TiO_2 films. The two intermediate layers were first deposited with 20 ALD cycles in order to form a complete coverage of the CNT surface. Then, TiO_2 with 100 and 300 ALD cycles was deposited on the bare CNTs, Al_2O_3, and ZnO intermediate layers at 240 °C, respectively. The aim of these experiments is to control the microstructure of the TiO_2 films by simply modifying the different intermediate layers.

The morphology and microstructure of all the TiO_2-coated CNTs, Al_2O_3/CNTs and ZnO/CNT samples were thoroughly investigated by TEM. Figure S1 of the Supporting Information shows TEM images of the TiO_2/CNT samples with different number of ALD cycles at 120 and 160 °C. Both the deposition temperature and the number of ALD cycles play a critical role in the film morphology and crystallization. TiO_2 film is smooth and amorphous at low temperature (120 °C; Figure S1a–c, Supporting Information), whereas it starts to crystallize at higher temperature (160 °C; Figure S1d,e, Supporting Information), as confirmed by the diffuse reflections in the selected area electron diffraction (SAED) pattern on top of the reflections of the CNTs (Figure S1f, Supporting Information, red labels), although the coating remains conformal. On the other hand, with the increase of the number of cycles, the formation of highly crystalline triangular particles can be clearly observed on top of a conformal pseudoamorphous TiO_2 film similar to the one obtained after 100 cycles (Figure S1g–i, Supporting Information). **Figure 2** shows HRTEM images of TiO_2 deposited on CNTs after 20, 100, and 300 cycles at 240 °C. A very thin granular TiO_2 layer is obtained (Figure 2a,b) after 20 cycles

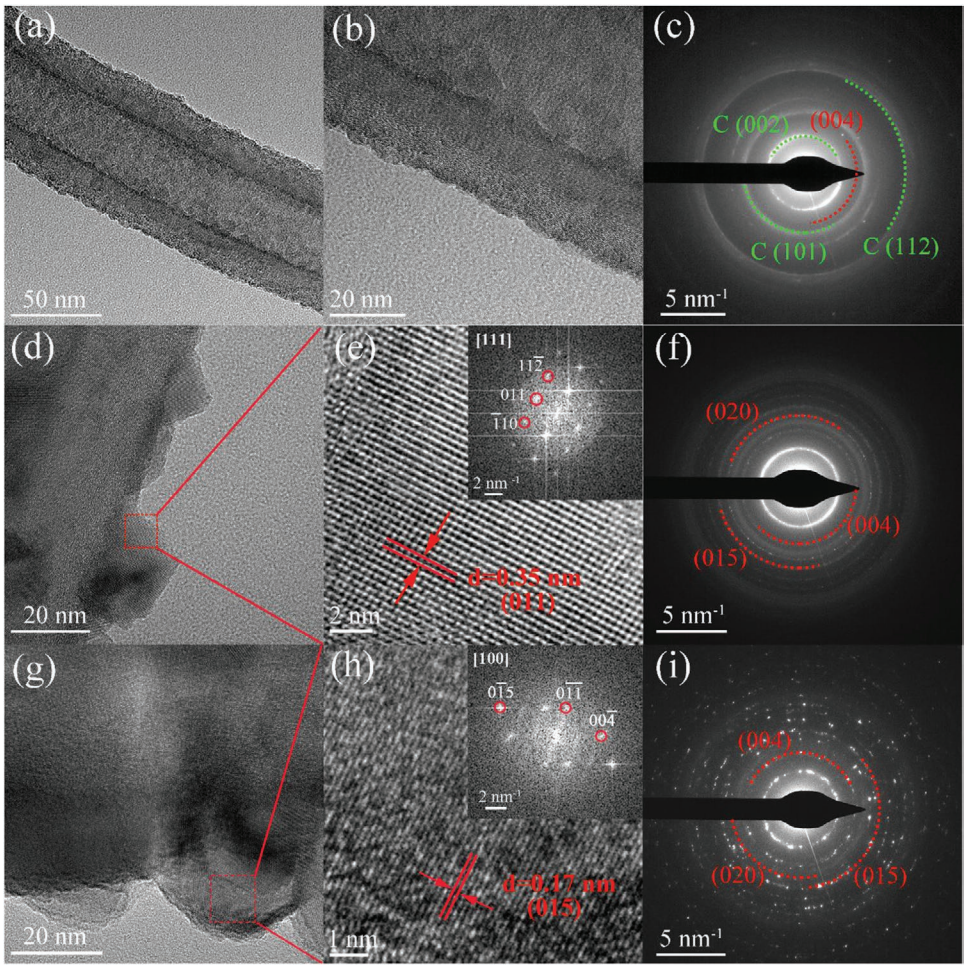

Figure 2. HRTEM images of TiO_2 deposited at 240 °C on CNTs with different ALD cycles: a,b) HRTEM images for TiO_2-20/CNTs. c) Corresponding SAED pattern of TiO_2-20/CNTs. d,e) HRTEM images for TiO_2-100/CNTs and the magnified view of the lattice fringes. The inset in (e) shows the corresponding power spectrum. f) Corresponding SAED pattern of TiO_2-100/CNTs. g,h) HRTEM images for TiO_2-300/CNTs and the magnified view of the lattice fringes. The inset in (h) shows the corresponding power spectrum. i) Corresponding SAED pattern of TiO_2-300/CNTs.

made of small nanocrystallites as also demonstrated by the diffuse reflections in the SAED pattern (Figure 2c, red labels). The main rings in the SAED correspond to the (002), (101), and (112) planes for graphitized carbon (COD 96-101-1061, green labels), but reflections attributed to anatase (COD 96-720-6076, red labels) are also present. The number of ALD cycles needed for initiation of crystallization of TiO_2 films on CNTs is around 60, which can be verified by XRD results (Figure S2, Supporting Information). Correspondingly, the critical thickness is about 3 nm, as shown in TEM images (Figure S3, Supporting Information). With increasing the number of ALD cycles, crystalline triangular particles appear within the amorphous film (Figure 2d; Figure S4a, Supporting Information). After 300 ALD cycles, the large crystalline particles begin to coalesce together and a rough film made of triangular crystallites is obtained (Figure 2g; Figure S4b, Supporting Information). The HRTEM images of part of single crystallites are displayed in Figure 2e,h. Their power spectra (PS, cf. insets) correspond to the [111] and [100] zone axis of the anatase TiO_2 structure, respectively. The SAED patterns in Figure 2f,i (red labels) indicate that the TiO_2 coating is polycrystalline. The phase composition and structure of TiO_2-100/CNTs and TiO_2-300/CNTs were further confirmed by XRD (Figure S5, Supporting Information). The distinct diffraction peaks located at 25.30°, 37.77°, and 48.04° can be attributed to the (011), (004), and (020) reflections of anatase TiO_2, respectively. In addition, the reflections at 26.23° marked with stars are assigned to the (002) plane of graphitic carbon in the CNTs.

Four different growth modes can be observed in thin film growth, namely, the Frank-van der Merwe growth (2D or layer-by-layer growth), random deposition, Volmer–Weber growth (island growth) and a combination of 2D growth and island growth, which is known as Stranski–Krastanov mode.[18] Based on the transmission electron microscopy study, we suggest that the growth of the TiO_2 film follows the Stranski–Krastanov mode, similarly to what was reported for TiN and GaN films grown by ALD.[19] Notably, the growth modes of different thin films are mainly governed by the surface energy, the strain energy and the interface energy.[13a,20] The deposited films will have a layer-by-layer (Frank–van der Merwe) growth pattern when $\gamma_s - \gamma_f - \gamma_i - \gamma_e \geq 0$, where γ_s, γ_f, γ_i, and γ_e represent the substrate surface free energy, the film surface free energy, the

interface free energy and the film strain energy, respectively. Thus, it becomes easier for a layer-by-layer growth mode to occur as the surface free energy of the substrate increases. Moreover, the deposited film will nucleate as an island-like (Volmer–Weber) growth if $\gamma_s - \gamma_f - \gamma_i - \gamma_e < 0$.[13a]

It is further accepted that the strain energy increases with the increase of the film thickness during the growth process owing to the inherent stiffness of the film.[13a] At the early stage of the growth, it can be seen that TiO_2 is strongly influenced by the underlying substrate to form a continuous pseudoamorphous layer (Figure 2a,b). For a larger number of ALD cycles, the strain energy progressively increases up to a critical thickness, when it is reached the nucleation of islands takes place (Figure 2d; Figure S4a, Supporting Information).[13a,20] This suggests that the influence of the underlying substrate gradually decreases and the system thermodynamically favors the release of the strain energy by the nucleation of islands. Finally, at even higher ALD cycles, the islands coalesced together as can be seen in the TiO_2/CNTs with 300 ALD cycles (Figure 2g; Figure S4b, Supporting Information).[20,21]

2.2. Effects of Intermediate Layers on the Growth Process of TiO_2 on CNTs

Figure S6 in the Supporting Information shows the HRTEM images of Al_2O_3 and ZnO films deposited on CNTs with 20 ALD cycles, respectively. Both films (≈4 nm in thickness) are smoothly and homogenously deposited onto the CNTs. The Al_2O_3 film is amorphous while the ZnO film shows a crystalline wurtzite structure. **Figure 3** presents the TEM images of TiO_2 deposited with 100 ALD cycles at 240 °C with Al_2O_3 and ZnO intermediate layers. In contrast to TiO_2 grown on bare CNTs, TiO_2 on Al_2O_3 and ZnO (Figure 3a,b,f,g) show a more conformal and homogeneous morphology. The HAADF-STEM images and the corresponding elemental mapping reveal a smooth and uniform TiO_2 deposition on the Al_2O_3 and ZnO surfaces with approximate thicknesses of 12.5 and 8.8 nm, respectively. The color-coded elemental maps show an even distribution of all elements, further indicating the presence of a homogenous coverage (Figure 3d,e,i,j). Hence, Al_2O_3 and ZnO intermediate layers can lead to a smooth layer at the early

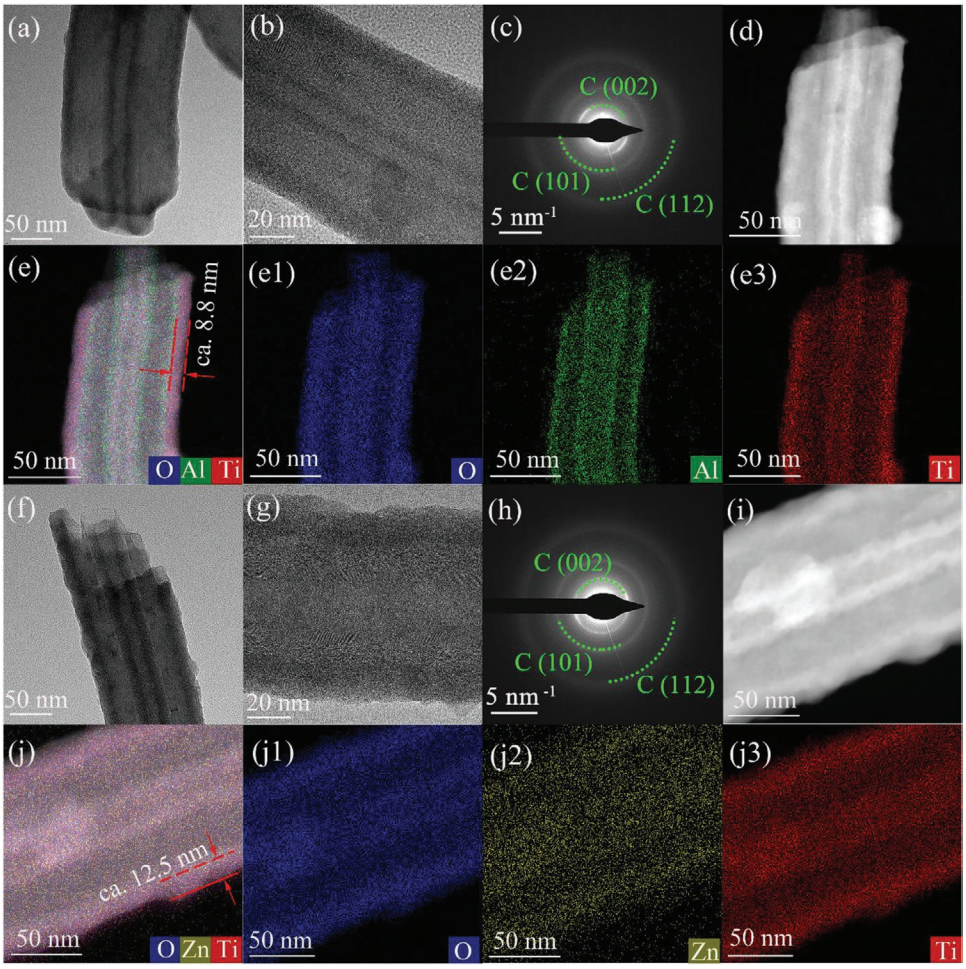

Figure 3. TEM images of the samples with 100 ALD cycles of TiO_2 deposited at 240 °C on CNTs with two different intermediate layers a,b) Al_2O_3 and f,g) ZnO. c,h) Corresponding SAED patterns of TiO_2-100/Al_2O_3/CNTs and TiO_2-100/ZnO/CNTs. d,e) HAADF-STEM images of TiO_2-100/Al_2O_3/CNTs and the corresponding EDX elemental maps for oxygen, aluminum, titanium and all combined elements, respectively. i,j) HAADF-STEM images of TiO_2-100/ZnO/CNTs and the corresponding EDX elemental maps for oxygen, zinc, titanium and all combined, respectively. The thickness marked in (e) and (j) are calculated with the Velox software.

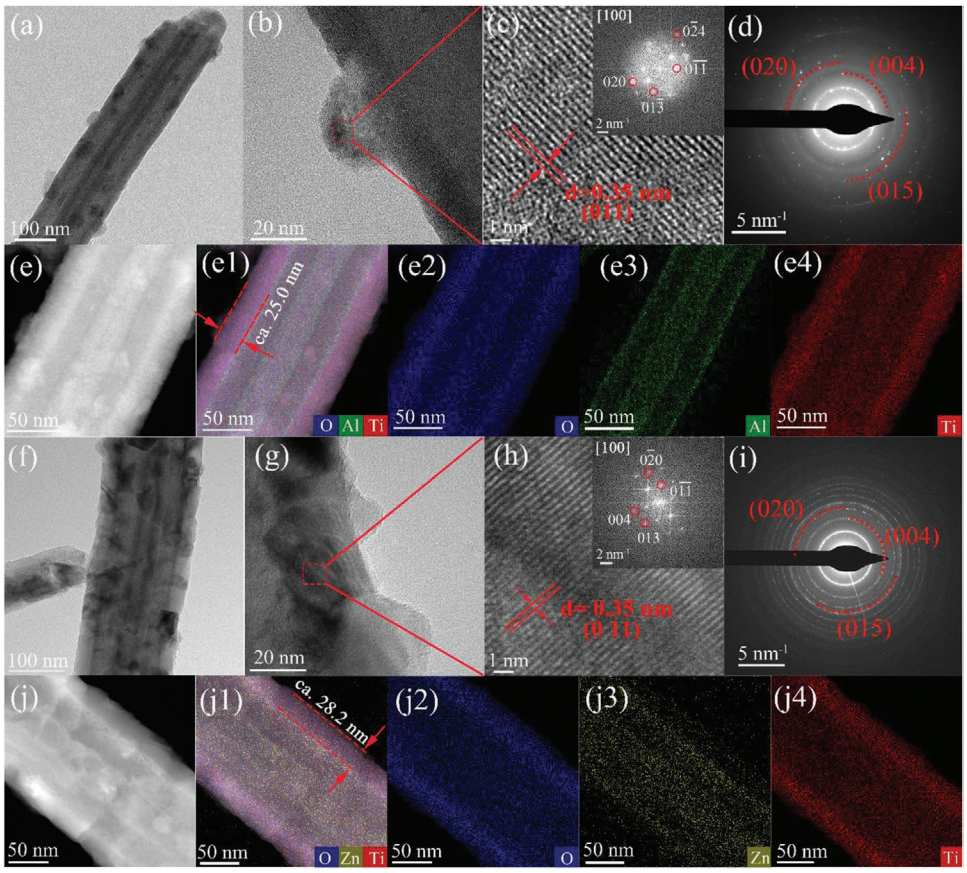

Figure 4. TEM images of a,b) TiO_2-300/Al_2O_3/CNTs and f,g) TiO_2-300/ZnO/CNTs. c) Magnified view of the lattice fringes for TiO_2-300/Al_2O_3/CNTs. The inset in (c) shows the corresponding power spectrum. d,i) SAED patterns from the corresponding samples. e) HAADF-STEM images of TiO_2-300/Al_2O_3/CNTs and the corresponding EDX elemental maps. h) Magnified view of the lattice fringes for TiO_2-300/ZnO/CNTs. The inset in (h) shows the corresponding power spectrum. j) HAADF-STEM images of TiO_2-300/ZnO/CNTs and the corresponding EDX elemental maps. The thickness marked on panels (e1) and (j1) are calculated with the Velox software.

growth stage. The reflections observed in the SAED patterns (Figure 3c,h, green labels) corresponding to TiO_2-100/Al_2O_3/CNTs and TiO_2-100/ZnO/CNTs, respectively, can be indexed to the CNTs, indicating the amorphous structure of deposited TiO_2 films. This shows that the crystallization did not start in the first 100 ALD cycles, in contrast to what happened on the bare CNTs where we clearly observed crystallites after 100 ALD cycles at the same growth temperature (cf. Figure 2d). Figure S5 in the Supporting Information shows the XRD patterns of the TiO_2-100/Al_2O_3/CNTs and TiO_2-100/ZnO/CNT samples. In contrast to TiO_2-100/CNTs which shows clear reflections attributed to the anatase phase, the TiO_2 films deposited on Al_2O_3 and ZnO intermediate layers are amorphous. In addition, any reflection corresponding to the Al_2O_3 and ZnO phases cannot be observed, which may be attributed to the intrinsic amorphous characteristic of Al_2O_3 film deposited by ALD[22] and the low mass loading of the ZnO thin layer after 20 ALD cycles.

To investigate the TiO_2 crystallization process further, the study was carried out with 300 TiO_2 ALD cycles while keeping the remaining deposition parameters constant. Both of the samples (TiO_2 deposited on Al_2O_3/CNTs and ZnO/CNTs) show conformally coated TiO_2 films onto the Al_2O_3 and ZnO intermediate layers (**Figure 4**). The TEM images for TiO_2-300/Al_2O_3/CNTs show the presence of few crystalline triangular particles on a conformal TiO_2 film of 25 nm in thickness (Figure 4a,e). The HRTEM image of a typical TiO_2 nanoparticle is shown in Figure 4b. The HRTEM and corresponding PS (Figure 4c) demonstrate the single crystalline nature of the particle and its orientation along the [100] direction. The SAED pattern of TiO_2-300/Al_2O_3/CNTs confirms the polycrystalline characteristic of the TiO_2 coating (Figure 4d, red labels). The HAADF-STEM and the corresponding elemental maps further show a homogenous distribution of Ti, Al, and O elements throughout the inner and outer walls of the CNTs (Figure 4e). TiO_2 was also conformally deposited on the ZnO intermediate layer. The TEM and HRTEM images of TiO_2-300/ZnO/CNTs reveal the presence of crystalline regions within the TiO_2 film of 28 nm in thickness (Figure 4f–h). The SAED pattern (Figure 4i, red labels) confirms that a polycrystalline anatase TiO_2 film is deposited onto ZnO. The HAADF-STEM images and the corresponding elemental maps confirm these findings (Figure 4j). These results indicate that a higher thickness is required for the initiation of the TiO_2 crystallization in the presence of an Al_2O_3 or ZnO intermediate layer, compared to bare CNTs, ultimately leading to conformal anatase thin films. Besides, it also suggests that the crystallization and growth behavior of TiO_2

Table 1. Summarized surface properties of different substrates with CNTs.

Sample	Contact angle [°][a]		Surface energy [mJ m^{-2}]		
	DI water	DIM	Dispersive (γ_{sg}^{d})	Polar (γ_{sg}^{p})	Surface (γ_{sg})
CNTs	121.3	35.1	42.0	3.2	45.2
Al_2O_3/CNTs	48.4	20.4	47.7	15.7	63.4
ZnO/CNTs	127.3	24.8	46.2	5.9	52.1

[a]Contact angle is determined from the average value of fifteen measurements.

films are closely related to the type of substrates. Compared to Al_2O_3, ZnO facilitates the growth of a polycrystalline and conformal TiO_2 film. Further discussion on this behavior can be found below in the next section.

The crystalline structure of the samples was confirmed by XRD (Figure S5, Supporting Information). The crystallite sizes were estimated using the Scherrer formula based on two specific crystalline planes of (011) and (020) as 22.8, 12.4, and 27.4 nm for TiO_2-300/CNTs, TiO_2-300/Al_2O_3/CNTs and TiO_2-300/ZnO/CNTs, respectively. This result indicates that although a comparable crystallite size for the TiO_2/CNTs and the TiO_2/ZnO/CNT system after 300 cycles is obtained, in the first case the coating is rough and composed of triangular crystallites while in the latter a very nice and conformal polycrystalline film is obtained.

2.3. Growth Mechanism

As described in the previous sections, the microstructure and crystallinity of the TiO_2 films in all of these samples, namely TiO_2/CNTs nanocomposites without and with the intermediate layers (Al_2O_3 and ZnO), are quite different. Without the intermediate layers, islands nucleate from a pseudoamorphous TiO_2 film once its thickness exceeded a critical value of few nanometers and a very rough film made of triangular crystallites was obtained with increasing the number of ALD cycles. On the other hand, a phase transition from amorphous to crystalline anatase TiO_2 was delayed with the use of Al_2O_3 and ZnO intermediate layers, ultimately leading to nicely conformal polycrystalline anatase TiO_2 films. So, we could demonstrate that the morphology and crystallization of the ALD-grown films are strongly dependent on the substrate. For a 2D growth, it is known that the surface energy of the substrate must be higher than the sum of the surface energy of the film, the film strain energy and the interface energy.[13a] This suggests that the surface energy plays a significant role in the growth of TiO_2 film by ALD and that the increase of the surface energy of the substrate can facilitate the occurrence of layer-by-layer growth at the initial growth stage.

The surface energy of the CNTs, Al_2O_3, and ZnO reported in the literature (Table S1, Supporting Information) indicates that the CNTs have much lower surface energy than Al_2O_3 and ZnO surfaces. Since different surface energies could induce different crystallization and growth behaviors, the surface energies of pure CNTs, Al_2O_3, and ZnO intermediate layers used in this study were estimated. The surface energy was determined by measuring the contact angles of two liquids, deionized (DI) water and diiodomethane (DIM). The surface energy γ_{sg} can be calculated by Equation (1)[23]

$$(1+\cos\theta)\gamma_{lg} = 2\left(\gamma_{sg}^{d}\gamma_{lg}^{d}\right)^{0.5} + 2\left(\gamma_{sg}^{p}\gamma_{lg}^{p}\right)^{0.5} \quad (1)$$

where θ is the contact angle, γ_{sg} is the total surface energy of the solid of interest, and γ_{lg} is the liquid–gas interface free energy. The superscripts d and p represent the dispersive and the polar components of the surface energy, respectively.

The surface energy parameters of the CNTs are calculated by applying the OWRK model (the one according to Owens, Wendt, Rabel, and Kaelble)[24] and are summarized in **Table 1**. Note that DIM is the standard dispersive liquid for surface free energy determination, due to its nonpolar nature, while water is often utilized as the polar liquid due to its polar nature. The contact angles of DI water and DIM droplets deposited on the surface are shown in **Figure 5**. The CNTs and ZnO/CNT films exhibit

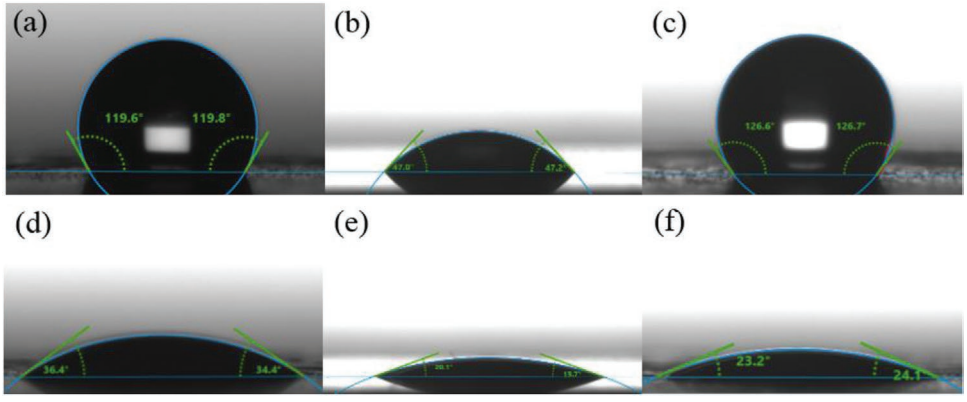

Figure 5. Contact angles of a–c) DI water and d–f) DIM droplets on the surface of a,d) CNTs, b,e) Al_2O_3/CNTs, and c,f) ZnO/CNTs.

large water contact angles of 121.3° and 127.3°, respectively (Figure 5a,c). In contrast to a hydrophobic surface of these two samples, the water contact angle of Al_2O_3/CNTs is 48.4°, suggesting a hydrophilic surface (Figure 5b). The contact angles of CNTs, Al_2O_3/CNTs and ZnO/CNT films obtained by using DIM are 35.1°, 20.4°, and 24.8°, respectively (Figure 5d–f). According to the separation of interfacial tension, the underlying interactions between the molecules include polar and dispersive interactions. The total surface energy of solid is determined by the sum of polar and dispersive parts.[23] The calculated total surface energies of CNTs, Al_2O_3/CNTs, and ZnO/CNT films are 45.2, 63.4, and 52.1 mJ m^{-2}, respectively. This result indicates that Al_2O_3 and ZnO intermediate layers have higher surface energy than the CNTs, which is consistent with the reported data from the literature (Table S1, Supporting Information). Therefore, the TiO_2 film should grow more conformally on the Al_2O_3 and ZnO intermediate layers in order to minimize the total energy of the system. Compared to bare CNTs, Al_2O_3, and ZnO intermediate layers facilitate 2D film growth at the initial stage and the subsequent film growth can more likely follow the initial conformal morphology, which leads to nicely smooth TiO_2 coatings. Moreover, the substrates with a high surface energy can delay the crystallization of TiO_2 films. This is supported by the result that a higher thickness is required to initiate the TiO_2 crystallization onto Al_2O_3 and ZnO intermediate layers. As a matter of fact, a very rough TiO_2 film made of triangular crystallites was obtained on CNTs (Figure 2g), whereas conformal and crystalline TiO_2 films (Figure 4a,f) are obtained on modified CNTs with Al_2O_3 and ZnO intermediate layers. Finally, when comparing the two intermediate layers the difference in conformality and crystallinity of the anatase film may result from i) the lower surface energy of ZnO promoting the crystallization process, and ii) the fact that Al_2O_3 is amorphous, but ZnO is crystalline which has an effect on the film strain energy.

It is worth noting that the film morphology and crystallinity of TiO_2 materials are significant for various practical applications. For instance, amorphous TiO_2 films possess both high ion diffusion rate and high electrochemical capacity in energy storage and conversion applications.[2c] Crystalline TiO_2 particles are also favorable for photocatalysis, since they can improve the total surface area and the efficiency of light absorption.[5] Moreover, the precise control of the TiO_2 coating thickness by ALD is beneficial for optimizing charge transport in photocatalysis systems.[2b] In this work, the photocatalytic efficiency of TiO_2-300/CNTs, TiO_2-300/Al_2O_3/CNTs, and TiO_2-300/ZnO/CNTs are evaluated by the degradation of Methyl Orange (Figure S7, Supporting Information). Among them, TiO_2-300/CNTs shows the highest efficiency due to its high crystallinity, which is one of crucial factors that affecting the photogenerated electron–hole recombination rate.[25] The photocatalytic efficiency decreases in the case of Al_2O_3 and ZnO intermediate layers due to the delayed crystallization of TiO_2 films. Compared to TiO_2-300/Al_2O_3/CNTs, TiO_2 films deposited on the ZnO intermediate layer exhibit some photocatalytic activity. These results show that the photocatalytic activity can be optimized with suitable intermediate layers. Moreover, these TiO_2/CNT-based nanocomposites are not only limited to the field of photocatalysis, but can also be used for electronic/optoelectronic devices such as transistors and beyond.

3. Conclusion

In summary, the role of Al_2O_3 and ZnO intermediate layers in the crystallization and growth behavior of ALD TiO_2 on CNTs has been systematically investigated. It was found that TiO_2 on bare CNTs begins to grow as a conformal amorphous film, and then highly crystalline triangular TiO_2 particles appeared after the amorphous film exceeded a critical thickness. Finally, a very rough TiO_2 film made of triangular crystallites was obtained with further increasing the number of ALD cycles. Al_2O_3 and ZnO intermediate layers, exhibiting a higher surface energy, can delay the crystallization of TiO_2 and ultimately facilitate the growth of conformal and crystalline TiO_2 films. Our findings demonstrate that the microstructure and the morphology of the TiO_2 coating strongly depends on the substrate properties despite they are grown under the same conditions. This indicates that the crystallization behavior is governed by the interface between the substrate and the film. ALD of Al_2O_3 and ZnO intermediate layers provide a practical way to control the interface and the coating on curved substrates and even high aspect ratio nanostructures, which is promising for the design and fabrication of heterostructures for a variety of applications.

4. Experimental Section

Materials: CNTs and nitric acid (HNO_3, 67%) were purchased from Applied Science (pyrograf III, PR24-PS) and VWR Chemicals, respectively. Titanium tetrachloride ($TiCl_4$, 99%) was provided by ABCR GmbH. Ozone was produced by a BMT803N ozone delivery system using pure oxygen at a pressure of 0.5 bar, and nitrogen (99.99%) was purchased from Air Liquide. Diethylzinc ($(C_2H_5)_2Zn$, DEZ, 95%) and trimethylaluminum ($(CH_3)_3Al$, TMA, 98%) were purchased from Sigma Aldrich and STREM Chemicals, respectively. All other chemicals and reagents were of analytical grades.

Pretreatments on CNTs: The CNTs were oxidized in HNO_3. In detail, 2 g of as-received CNTs were dispersed in 80 mL of concentrated HNO_3 in a round-bottom flask, and then the dispersion was stirred and refluxed at 105 °C in an oil bath for 6 h. The dispersion was filtered and washed many times with distilled water until pH = 7. The functionalized CNTs were collected and dried in oven at 60 °C overnight. For the ALD depositions, the CNTs were drop-casted on a well-cleaned aluminum foil from a homogeneous dispersion in ethanol.

ALD of TiO_2: TiO_2 was deposited on CNTs and Si wafers using a PLAY 2018-01 (CTECHnano) thermal ALD system. The ALD system was evacuated and the temperature was well stabilized before starting the deposition. The baseline pressure was maintained at 7.3×10^{-1} mbar with a 40 sccm of nitrogen flow. High purity nitrogen was used as both the purging and carrier gas. $TiCl_4$ and H_2O were used as the metal precursor and the oxygen source, respectively. $TiCl_4$ and H_2O were maintained in stainless steel canisters at room temperature. The temperatures of the manifold and the reaction chamber were maintained at 100 and 240 °C, respectively. Each ALD cycle consisted of a 0.05 s $TiCl_4$ pulse, 50 s exposure time, 30 s N_2 purge, 0.15 s pulse of H_2O, 40 s exposure time, and 30 s of N_2 purge. The samples were deposited with 100 and 300 ALD cycles, and named as TiO_2-100/CNTs and TiO_2-300/CNTs, respectively. Other ALD processes were carried out by depositing Al_2O_3 and ZnO intermediate layers prior to the growth of TiO_2 films.

ALD of Al_2O_3: Al_2O_3 was deposited on CNTs using a PLAY 2018-01 (CTECHnano) thermal ALD system. The pressure of the reaction chamber is the same as for the ALD of TiO_2. Al_2O_3 was deposited using TMA and H_2O. The temperature of the ALD chamber was maintained at

180 °C. All other reactor parameters were kept the same as for the ALD process of TiO_2. Both the precursors were kept at room temperature and pulsed alternatively each for 0.05 s pulse, and separated by a 30 s exposure and 30 s N_2 purging time. 20 cycles of Al_2O_3 were carried out and the samples were named as Al_2O_3/CNTs.

ALD of ZnO: Functionalized CNTs were coated with ZnO by ALD using a hot-wall GEMSTAR-6 Benchtop ALD system (ARRADIANCE, Inc.). The baseline pressure was maintained at 2.0×10^{-1} torr with a 10 sccm of argon flow. ZnO was deposited using DEZ and H_2O. The temperature of the ALD chamber was maintained at 120 °C. All other reactor parameters were kept the same as for the ALD process of TiO_2. DEZ and H_2O were kept at room temperature, whereas the pulses of DEZ and H_2O were adjusted to 0.05 and 0.1 s, respectively. The exposure and purging time for both DEZ and H_2O steps were set to 30 s. 20 cycles of ZnO were carried out and the samples were named as ZnO/CNTs.

Characterization: High-resolution transmission electron microscopy (HRTEM), high-angle annular dark-field scanning transmission electron microscopy (HAADF-STEM) and energy dispersive X-ray analysis (EDX) elemental mapping were carried out on a FEI Talos F200S scanning/transmission electron microscope (S/TEM) at an acceleration voltage of 200 kV. Transmission electron microscopy (TEM) was also carried out on a Philips CM 200S equipped with a LaB_6 filament. X-ray diffraction (XRD) patterns were acquired on a STOE MP XRD with Cu Kα1 radiation ($\lambda = 1.5400$ Å) in transmission configuration at 40 kV, 100 mA.

Contact Angle Measurements: Contact angle measurements were performed by a KRÜSS Drop Shape Analyzer using the sessile drop method. The contact angles for Al_2O_3 and ZnO were measured with CNTs as a support, for this, a film based on CNTs was deposited by spin coating. CNTs were dispersed in ethanol and a droplet was placed on a cleaned Si wafer which was fixed on a spin coater at a rotating speed of 1700 rpm for 30 s. The process was repeated ten times until a smooth CNT film was formed after drying. Al_2O_3/CNTs and ZnO/CNT films were obtained by depositing 20 ALD cycles of Al_2O_3 and ZnO on the CNT film, respectively.

Supporting Information

Supporting Information is available from the Wiley Online Library or from the author.

Acknowledgements

J. Wang acknowledges the fellowship from the China Scholarship Council (CSC). Z. Yin appreciates the visiting research fellowship from Deutscher Akademischer Austauschdienst (DAAD) and the support from Natural Science Foundation of Fujian Province for Distinguished Young Scholars (No. 2019J06023). M. Hamid Raza is acknowledged for assistance with ALD experiments. P. Hänsch is acknowledged for assistance with contact angle measurements. C. Erdmann is acknowledged for the TEM measurement. M. Trunk is acknowledged for the photocatalytic tests. Y. Liu is acknowledged for drawing the schematic diagram.

Open access funding enabled and organized by Projekt DEAL.

Conflict of Interest

The authors declare no conflict of interest.

Data Availability Statement

The data that support the findings of this study are available from the corresponding author upon reasonable request.

Keywords

Al_2O_3, atomic layer deposition, carbon nanotubes, inorganic interfaces, TiO_2, ZnO

Received: May 11, 2021
Revised: June 8, 2021
Published online: July 11, 2021

[1] a) P. Kaushik, M. Eliáš, J. Michalička, D. Hegemann, Z. Pytlíček, D. Nečas, L. Zajíčková, *Surf. Coat. Technol.* **2019**, *370*, 235; b) K. Woan, G. Pyrgiotakis, W. Sigmund, *Adv. Mater.* **2009**, *21*, 2233.

[2] a) C. Marichy, N. Donato, M. Latino, M. G. Willinger, J. P. Tessonnier, G. Neri, N. Pinna, *Nanotechnology* **2015**, *26*, 024004; b) S. H. Huang, S. Y. Liao, C. C. Wang, C. C. Kei, J. Y. Gan, T. P. Perng, *Nanotechnology* **2016**, *27*, 405702; c) M. Xie, X. Sun, C. Zhou, A. S. Cavanagh, H. Sun, T. Hu, G. Wang, J. Lian, S. M. George, *J. Electrochem. Soc.* **2015**, *162*, A974.

[3] C. Marichy, N. Pinna, *Coord. Chem. Rev.* **2013**, *257*, 3232.

[4] a) C. Marichy, J.-P. Tessonnier, M. C. Ferro, K.-H. Lee, R. Schlögl, N. Pinna, M.-G. Willinger, *J. Mater. Chem.* **2012**, *22*, 7323; b) C.-Y. Hsu, D.-H. Lien, S.-Y. Lu, C.-Y. Chen, C.-F. Kang, Y.-L. Chueh, W.-K. Hsu, J.-H. He, *ACS Nano* **2012**, *6*, 6687.

[5] S.-H. Huang, C.-C. Wang, S.-Y. Liao, J.-Y. Gan, T.-P. Perng, *Thin Solid Films* **2016**, *616*, 151.

[6] a) N. Duraisamy, N. M. Muhammad, H.-C. Kim, J.-D. Jo, K.-H. Choi, *Thin Solid Films* **2012**, *520*, 5070; b) S. Naseem, I. V. Pinchuk, Y. K. Luo, R. K. Kawakami, S. Khan, S. Husain, W. Khan, *Appl. Surf. Sci.* **2019**, *493*, 691; c) K. Shalini, S. Chandrasekaran, S. A. Shivashankar, *J. Cryst. Growth* **2005**, *284*, 388; d) M. Buchalska, M. Surówka, J. Hämäläinen, T. Iivonen, M. Leskelä, W. Macyk, *Catal. Today* **2015**, *252*, 14; e) M. Gotić, M. Ivanda, A. Sekulić, S. Musić, S. Popović, A. Turković, K. Furić, *Mater. Lett.* **1996**, *28*, 225.

[7] a) S. M. George, *Chem. Rev.* **2010**, *110*, 111; b) R. W. Johnson, A. Hultqvist, S. F. Bent, *Mater. Today* **2014**, *17*, 236.

[8] N. Pinna, M. Knez, *Atomic Layer Deposition of Nanostructured Materials*, Wiley-VCH, Weinheim, Germany **2012**.

[9] a) C. Guerra-Nunez, Y. Zhang, M. Li, V. Chawla, R. Erni, J. Michler, H. G. Park, I. Utke, *Nanoscale* **2015**, *7*, 10622; b) J. R. Avila, S. B. Qadri, J. A. Freitas, N. Nepal, D. R. Boris, S. G. Walton, C. R. Eddy, V. D. Wheeler, *Chem. Mater.* **2019**, *31*, 3900.

[10] Y. Zhang, C. Guerra-Nuñez, I. Utke, J. Michler, M. D. Rossell, R. Erni, *J. Phys. Chem. C* **2015**, *119*, 3379.

[11] a) C. J. Cho, J.-Y. Kang, W. C. Lee, S.-H. Baek, J.-S. Kim, C. S. Hwang, S. K. Kim, *Chem. Mater.* **2017**, *29*, 2046; b) G. Luka, B. S. Witkowski, L. Wachnicki, M. Andrzejczuk, M. Lewandowska, M. Godlewski, *CrystEngComm* **2013**, *15*, 9949; c) R. Methaapanon, S. F. Bent, *J. Phys. Chem. C* **2010**, *114*, 10498; d) W.-J. Lee, M.-H. Hon, *J. Phys. Chem. C* **2010**, *114*, 6917; e) S. M. Ali, S. Al Salman, S. Al-Ghamdi, M. Al Garawi, M. Baig, T. S. Alkhuraiji, *J. Optoelectron. Adv. Mater.* **2016**, *18*, 666.

[12] a) Y. Liang, S. Gan, S. A. Chambers, E. I. Altman, *Phys. Rev. B* **2001**, *63*, 235402; b) D. R. G. Mitchell, D. J. Attard, G. Triani, *J. Cryst. Growth* **2005**, *285*, 208; c) S. K. Kim, G. W. Hwang, W.-D. Kim, C. S. Hwang, *Electrochem. Solid-State Lett.* **2005**, *9*, F5; d) S. Cong, X. Liu, Y. Jiang, W. Zhang, Z. Zhao, *Innovation* **2020**, *1*, 100051.

[13] a) O. Kitakami, S. Okamoto, Y. Shimada, *J. Appl. Phys.* **1996**, *79*, 6880; b) G. E. Testoni, W. Chiappim, R. S. Pessoa, M. A. Fraga, W. Miyakawa, K. K. Sakane, N. K. A. M. Galvão, L. Vieira, H. S. Maciel, *J. Phys. D* **2016**, *49*, 375301; c) K. S. Finnie,

G. Triani, K. T. Short, D. R. G. Mitchell, D. J. Attard, J. R. Bartlett, C. J. Barbé, *Thin Solid Films* **2003**, *440*, 109.
[14] J. G. Amar, F. Family, P. M. Lam, *Phys. Rev. B: Condens. Matter Mater. Phys.* **1994**, *50*, 8781.
[15] I. Kavre Piltaver, R. Peter, I. Šarić, K. Salamon, I. Jelovica Badovinac, K. Koshmak, S. Nannarone, I. Delač Marion, M. Petravić, *Appl. Surf. Sci.* **2017**, *419*, 564.
[16] R. L. Puurunen, T. Sajavaara, E. Santala, V. Miikkulainen, T. Saukkonen, M. Laitinen, M. Leskela, *J. Nanosci. Nanotechnol.* **2011**, *11*, 8101.
[17] X. Sun, M. Xie, J. J. Travis, G. Wang, H. Sun, J. Lian, S. M. George, *J. Phys. Chem. C* **2013**, *117*, 22497.
[18] R. L. Puurunen, *Chem. Vap. Deposition* **2004**, *10*, 159.
[19] a) C. Adelmann, J. Brault, J. L. Rouvière, H. Mariette, G. Mula, B. Daudin, *J. Appl. Phys.* **2002**, *91*, 5498; b) H. Van Bui, A. Y. Kovalgin, R. A. Wolters, *ECS J. Solid State Sci. Technol.* **2012**, *1*, P285.
[20] S. A. Chambers, *Surf. Sci. Rep.* **2000**, *39*, 105.
[21] S. K. Kim, S. Hoffmann-Eifert, M. Reiners, R. Waser, *J. Electrochem. Soc.* **2010**, *158*, D6.
[22] M. H. Raza, K. Movlaee, S. G. Leonardi, N. Barsan, G. Neri, N. Pinna, *Adv. Funct. Mater.* **2020**, *30*, 1906874.
[23] Y. Jiang, Z. Liu, Z. Yin, Q. Zheng, *Mater. Chem. Front.* **2020**, *4*, 1459.
[24] M. Annamalai, K. Gopinadhan, S. A. Han, S. Saha, H. J. Park, E. B. Cho, B. Kumar, A. Patra, S. W. Kim, T. Venkatesan, *Nanoscale* **2016**, *8*, 5764.
[25] J. M. Macak, M. Zlamal, J. Krysa, P. Schmuki, *Small* **2007**, *3*, 300.